ACS OMEGA

Open Access

This article is licensed under CC-BY-NC-ND 4.0

http://pubs.acs.org/journal/acsodf

Article

Structural Basis for the Improved RNA Clamping of Amidino-Rocaglates to eIF4A1

James F. Conley, Lauren E. Brown, James H. McNeely, Jerry Pelletier, John A. Porco, Jr,* and Karen N. Allen*

Cite This: *ACS Omega* 2025, 10, 5795−5808

Read Online

ACCESS | Metrics & More | Article Recommendations | Supporting Information

ABSTRACT: Eukaryotic initiation factor 4A-1 (eIF4A1) is an ATP-dependent RNA helicase that unwinds 5′-UTR mRNA secondary structures to facilitate cap-dependent translation initiation. Rocaglates, a class of natural products typified by rocaglamide A (RocA), possess antineoplastic and anti-infectious activity mediated by their interaction with eIF4A1. Rocaglates inhibit cap-dependent translation initiation by "clamping" eIF4A1 onto polypurine RNA, which impedes ribosome scanning. A novel class of rocaglate derivatives, amidino-rocaglates (ADRs) which feature an amidine ring fused to the rocaglate core, is particularly effective at promoting eIF4A1−RNA-clamping compared to other rocaglate congeners. Herein, we present the X-ray crystal structure of an ADR in complex with eIF4A1, the nonhydrolyzable ATP ground-state mimic adenylyl-imidodiphosphate (AMPPNP), and poly r(AG)$_5$ RNA refined to 1.69 Å resolution. The binding pose and interactions of the ADR with eIF4A1 do not differ substantially from those of RocA, prompting an investigation of the basis for enhanced target engagement. Computational modeling suggests that the rigidified ADR scaffold is inherently preorganized in an eIF4A1−RNA binding-competent conformation, thereby avoiding entropic penalties associated with RocA binding. This study illustrates how conformational rigidification of the rocaglate scaffold can be leveraged to improve potency for the development of rocaglates as potential anticancer and anti-infectious agents.

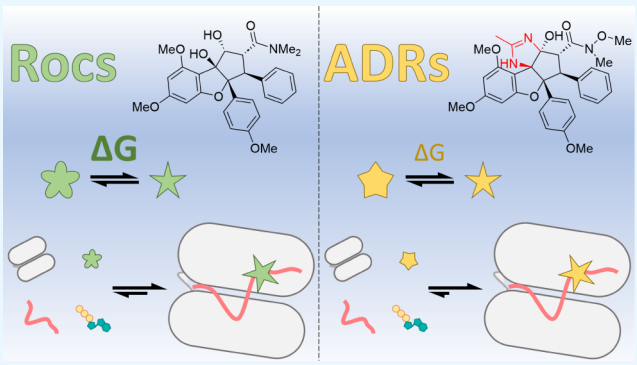

INTRODUCTION

Protein translation is arguably the most critical cellular process and is extensively regulated, requiring the involvement of dozens of proteins to modulate protein synthesis, both temporally and spatially. Translation is composed of three sequential steps: initiation, elongation, and termination. Initiation involves the recruitment of the cellular translation machinery to mRNA and is the primary point of regulation within the translation process.[1] The majority of eukaryotic initiation proceeds through a "cap-dependent" mechanism, denoted for the importance of the 5′-7-methylguanosine (m^7G) cap on the nascent mRNA strand for recognition by eukaryotic initiation factors (eIFs). Different mRNAs possess varying degrees of secondary structure that require the recruitment of eIFs to unwind the RNA and facilitate efficient ribosome scanning for the initiation codon by the 43S preinitiation complex (PIC). eIF4A is the RNA helicase responsible for unwinding the secondary structure in the 5′-untranslated regions (UTRs) of mRNAs and is a key component of the eIF4F cap-binding complex along with the 5′-m^7G cap-binding protein eIF4E and the scaffolding protein eIF4G.

In humans and most higher eukaryotes, there are three paralogues within the eIF4A subfamily of DEAD-box helicases: eIF4A1, eIF4A2, and eIF4A3. eIF4A1 is the predominant paralog involved in translation initiation, whereas eIF4A2 and eIF4A3 are involved in other processes related to mRNA metabolism.[2] eIF4A1 (DDX2A) and eIF4A2 (DDX2B) are very similar (90% sequence identity), and though they have been shown to be functionally interchangeable *in vitro*, the two proteins have distinct functions *in vivo* and are expressed at varying levels in different cell types.[3,4] Furthermore, overexpression of either eIF4A1 or eIF4A2 cannot compensate for the loss of the other for their respective functions.[5] eIF4A3 (DDX48) is more divergent and is functionally distinct from the other eIF4A paralogs.[2] eIF4A1 is one of the most ubiquitously expressed enzymes in eukaryotic cells and is a crucial node of the initiation step of eukaryotic cap-dependent

Received: October 15, 2024
Revised: January 23, 2025
Accepted: January 29, 2025
Published: February 10, 2025

© 2025 The Authors. Published by American Chemical Society

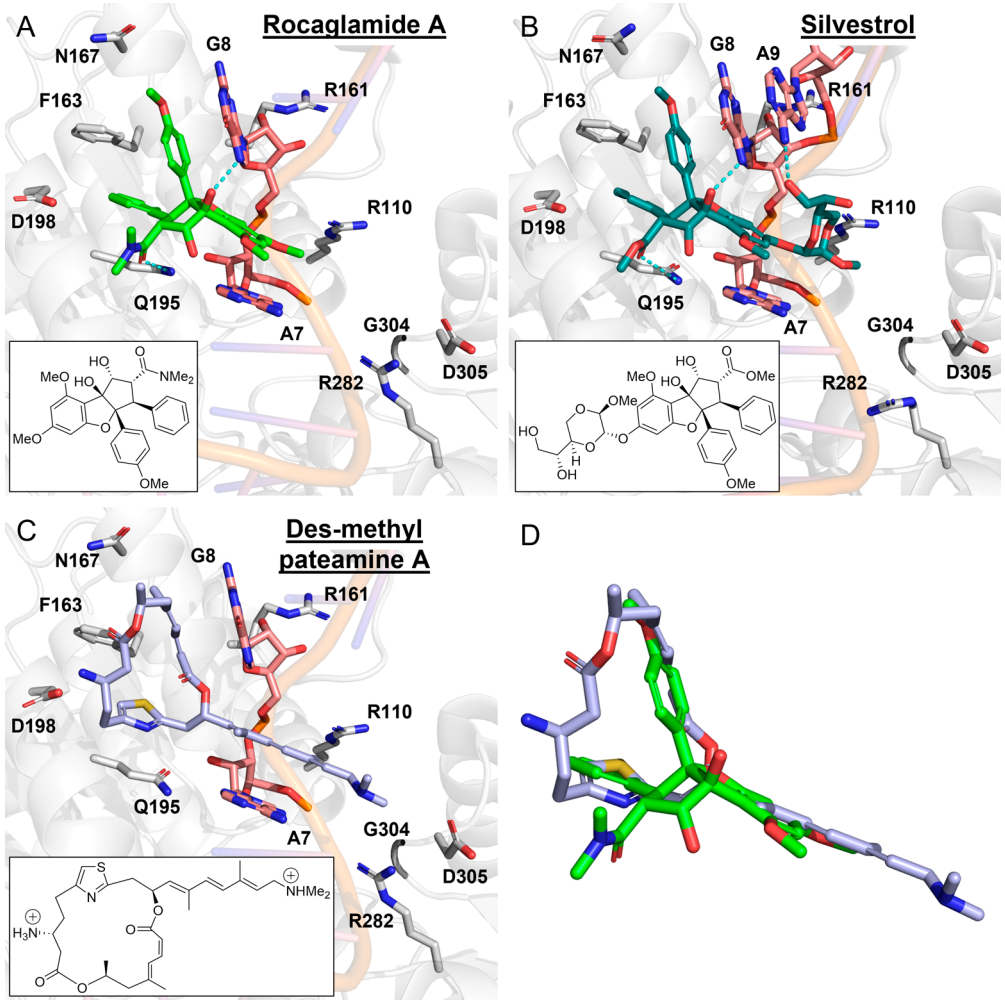

Figure 1. Comparison of the structures of eIF4A1:inhibitor complexes. (A) eIF4A1:RocA:RNA:AMPPNP complex from 5ZC9 with the corresponding chemical structure of RocA (inset).[21] (B) eIF4A1:silvestrol:RNA:AMPPNP complex from 9AVR with the corresponding chemical structure of silvestrol (inset).[22] Only one of the two conformations of the ethanediol substituent of the A-ring dioxanyloxy group is shown for clarity. (C) eIF4A1: DMPatA:RNA:AMPPNP complex from 6XKI with the corresponding structure of des-methyl pateamine A (DMPatA; MZ-735, inset).[23] Important residues for inhibitor binding are labeled. (D) RocA overlaid with DMPatA by the superposition of liganded structures.

translation.[6,7] Modulation of RNA unwinding through the direct regulation of eIF4A1 activity is a critical post-transcriptional means of not only modulating the rate of global protein translation but also regulating which mRNA transcripts are translated. eIF4A1 overexpression has been associated with poor outcomes in several cancers and, as a result, much of the recent research on it is contextualized by the investigation of its role in cancer and as a target for inhibition.[8]

Pharmacologic inhibition of eIF4A by several natural products, with varying degrees of specificity for the three paralogs, has been shown to have a potent antineoplastic effect in both *in vitro* and *in vivo* models of cancer.[5,8−12] Rocaglates are one example of a natural product class with a unique mechanism of selective inhibition of the translation of purine-rich mRNA mediated by their interaction with eIF4A1.[13−15] Rocaglates are a class of natural products of phytochemical origin that contain a cyclopenta[*b*]benzofuran core. The prototypical rocaglate, rocaglamide A (RocA), was first identified and isolated in 1982 from extracts of the plant *Aglaia elliptifolia*.[16] Since then, hundreds of related compounds, including silvestrol, have been isolated from various members of the genus *Aglaia*, and efficient syntheses have been developed to expand this chemical space (Figure S1).[17,18] Zotatifin (eFT226) is one example of a synthetic rocaglate shown to be an effective inhibitor of tumor growth in receptor tyrosine kinase-driven cancers and is currently being evaluated in the clinic as a component of combination therapies against estrogen receptor-positive metastatic breast cancer.[19,20]

Iwasaki and coworkers have published a pair of articles characterizing the mechanism of action of RocA, both biochemically and structurally.[15,21] RocA was shown to diminish protein production in a variety of model systems in a dose-dependent manner, with a notable difference in the magnitude of translational repression of 5′-UTRs containing high purine content. Such transcripts were found to be much more susceptible to translation repression by RocA than transcripts with 5′-UTRs containing elevated pyrimidine content.[15] The X-ray crystal structure of RocA bound to eIF4A1 and purine RNA revealed the rocaglate binding site at the interface of eIF4A1 and polypurine RNA, demonstrating how rocaglates force engagement between protein and RNA and lock the helicase into a closed conformation in a novel mechanism termed "clamping."[21] In this clamped state, eIF4A1

https://doi.org/10.1021/acsomega.4c09421
ACS Omega 2025, 10, 5795−5808

can no longer undergo the multiple rounds of RNA remodeling required for efficient start codon scanning by the 43S PIC, eIF4A1 is depleted from eIF4F, translation initiation is inhibited, and protein production in the cell is diminished.[15,21] The RNA sequence selectivity of rocaglates is thought to arise from π-stacking interactions between the rings A and B on the rocaglate core and consecutive purine nucleobases, along with a critical hydrogen bond between 8b-OH of RocA and N7 of a purine nucleobase, guanine 8 (G8) in the case of the published structure (Figures 1A and 2).[21] When polypyrimidine RNA is

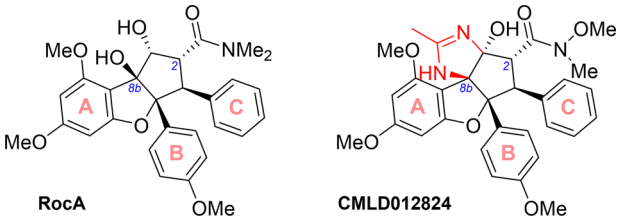

Figure 2. Chemical structure of RocA and ADR **CMLD012824**. RocA, the first rocaglate described, and **CMLD012824**, a potent derivative from a new class of compounds—amidino-rocaglates (ADRs)—share the same cyclopenta[*b*]benzofuran core with the A, B, and C rings labeled on each structure. ADRs feature an annulated heterocyclic amidine ring (shown in red) fused to the rocaglate scaffold. C2 and C8b, discussed in the text, are labeled in blue.

modeled in place of polypurine RNA, π-stacking interactions are misaligned and there is no hydrogen-bond acceptor for 8b-OH at the same location on the pyrimidine nucleobase.[21] This important structure showed additional details of target engagement, including a π-stacking interaction between the C ring of RocA and F163 and a hydrogen bond between the carbonyl of RocA's *C*2-*N*,*N*-dimethyl-carboxamide and the side-chain NH_2 group of Q195.[21]

A second structure of eIF4A1 bound to a rocaglate, the natural product silvestrol, was recently reported by Naineni and colleagues (Figure 1B).[22] Silvestrol, unlike most other rocaglates, can inhibit the translation of mRNAs that lack a high purine content in their 5′-UTRs, a phenomenon hypothesized to be explained by its unique dioxanyloxy moiety on the A-ring of the rocaglate scaffold. This new structure revealed that this group interacts with the subsequent adenine nucleobase (A9) of the poly$(AG)_5$ RNA oligonucleotide used in the crystallization experiment. Two alternative conformations of the methanediol substituent of this moiety were modeled in this structure, which can both potentially hydrogen bond to purine bases as observed in the crystal structure (*N*6 of adenine or *O*6 of guanine) or with pyrimidine nucleobases when modeled into the structure (*N*4 of cytosine or *O*4 of uracil).

Additionally, there is a published X-ray crystal structure of eIF4A1 bound to another translation inhibitor of a different chemical class, des-methyl pateamine A (DMPatA), a derivative of the marine sponge-derived natural product pateamine A (PatA).[23,24] Pateamines differ significantly from rocaglates in both chemical structure and pharmacophoric elements; these compounds are macrodiolides comprised of a decorated 19-membered ring fused to a thiazole heterocycle, with an additional large conjugated alkyl chain appended in a lariat-type structure. DMPatA differs from PatA by the removal of a single methyl group from the macrocycle. Despite a lack of structural similarity, DMPatA and RocA bind at the same location at the eIF4A1−RNA interface (Figure 1C).[23] The macrocycle of DMPatA occupies the same pocket as the B and C rings of RocA, while the conjugated alkyl chain occupies the same space as the A ring, while protruding further toward residues R282, G304, and D305 on the surface of eIF4A1 (Figure 1C,D). Notably, DMPatA does not have a unique interaction with purine nucleobases, explaining its superior capacity to inhibit translation of pyrimidine-rich mRNAs compared to RocA. Nevertheless, it does exhibit increased clamping activity for purine-rich mRNAs, similar to RocA; this difference can possibly be explained by the increased buried surface area arising from binding in complex with purine nucleotides.[23] As the authors describe in their title, DMPatA seems to exhibit a unique "functional mimicry" to rocaglates, suggesting that the stabilization of a preferred clamped orientation of RNA bound to eIF4A1 is of greater importance than the specific chemical structure of eIF4A-clamping inhibitors, like rocaglates or PatA analogs. These studies together suggest that diverse pharmacophores can be deployed to clamp RNA to eIF4A1 and inhibit downstream protein synthesis and that broad chemical space is available for the generation of helicase-interacting compounds that operate by a "clamping"-type mechanism.

We have previously reported amidino rocaglates (ADRs), a class of synthetic rocaglates with an amidine ring fused to the cyclopenta[*b*]benzofuran scaffold, which were serendipitously obtained from a retro-Nazarov reaction performed on a tosylated rocaglate core.[25] In our collaborative studies, ADRs were identified from a large-scale screen to have 2-fold greater eIF4A clamping to polypurine RNA when compared to prototypical rocaglates, as measured in fluorescence polarization assays, and exhibited potent cap-dependent translation inhibition.[26,27] Moreover, ADRs and a related guanidino rocaglate (GDR) were found to possess strong antiviral activity against hepatitis E virus (HEV) with EC_{50} values between 1 and 9 nM.[28] The strong potency of ADRs and emerging biology led us to undertake structural biology studies to probe the nature of the heightened target engagement.

Herein, we report the X-ray crystal structure, refined to 1.69 Å resolution, of an exemplar ADR, the potent translation inhibitor **CMLD012824**, in complex with eIF4A1, the nonhydrolyzable ATP analog adenylyl-imidodiphosphate (AMPPNP), and a poly r$(AG)_5$. This structural information combined with computational analysis suggests that conformational preorganization provided by the ADR-ring fusion is a key contributor to the enhanced activity of the rocaglate scaffold, suggesting new avenues for the development of inhibitory DEAD-box helicase ligands.

RESULTS AND DISCUSSION

Structure Determination of an ADR−eIF4A1−RNA−AMPPNP Cocrystal Complex. The main purpose of our investigation was to characterize the binding mode of ADRs and identify potential molecular determinants of their improved inhibition and target engagement of the eIF4A1−polypurine RNA interface. The ADR chosen for study was **CMLD012824**, an enantioenriched preparation of chiral, racemic **CMLD012612**, which is the most potent ADR identified to date.[26] To this end, we sought to determine the structure of the assumed quaternary complex formed by eIF4A1 bound to polypurine RNA, an ATP analogue, and the ADR. Each component of the quaternary complex is critical for the formation of a stable homogeneous crystallizable unit in

https://doi.org/10.1021/acsomega.4c09421
ACS Omega 2025, 10, 5795−5808

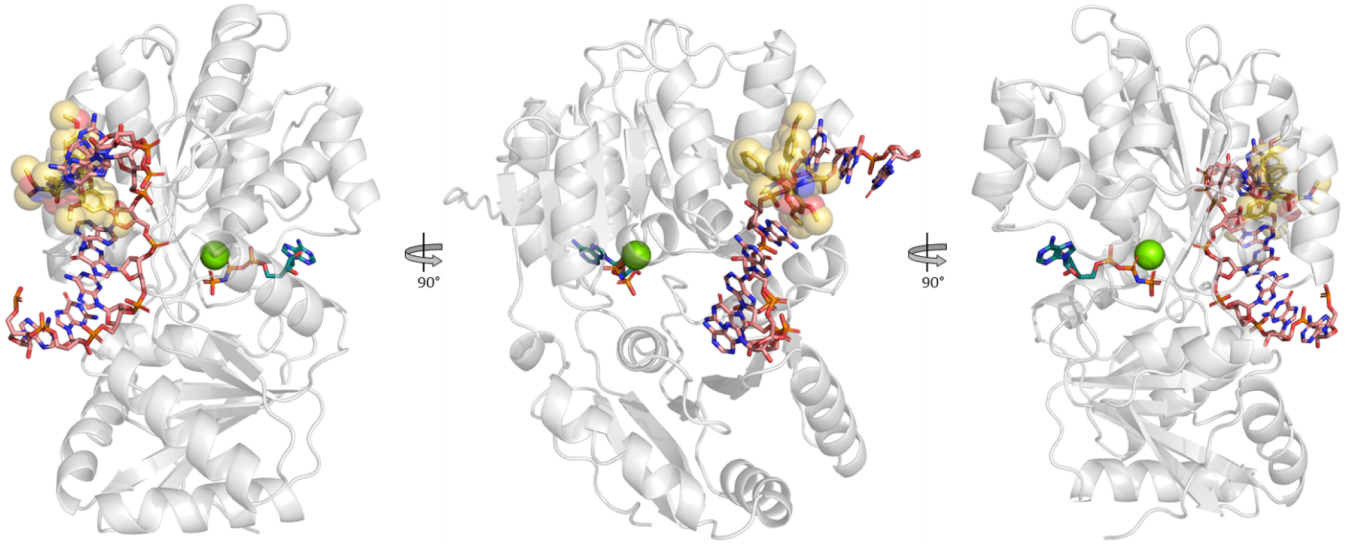

Figure 3. Structure of the eIF4A1:**CMLD012824**:RNA:AMPPNP quaternary complex. eIF4A1 shown as off-white transparent ribbon with poly$(AG)_5$ (salmon) **CMLD012824** (yellow stick with transparent spheres), AMPPNP (teal) shown as sticks, and Mg^{2+} as green sphere.

which eIF4A1 adopts and maintains a closed conformation. The previously reported structure of the RocA-bound quaternary complex was used as a reference for protein preparation. In that structure, HRV-3C-cleaved eIF4A1(19−406) was used for crystallization experiments; however, only residues 29−406 are well-resolved, offering the potential for more liberal truncation of the N-terminus. Based on this observation, we designed a smaller crystallization construct with a cleavable N-terminal SUMO-tag and a short -Ser-Ser- linker followed by residues 21−406. Rocaglates require the association of purine RNA to eIF4A1 for binding.[21] The polypurine RNA selected was poly r$(AG)_5$. eIF4A1, like other DEAD-box helicases, requires Mg^{2+}-ATP binding for RNA binding and ATP hydrolysis for successive unwinding events; thus, a nonhydrolyzable analog, AMPPNP, was included.[6,29,30] Poly r$(AG)_5$ and AMPPNP were each used in the published structure of RocA, so representing a reasonable starting point for this effort.

eIF4A1 crystallized in complex with **CMLD012824**, AMPPNP, and poly r$(AG)_5$ in the space group P1 with an asymmetric unit (ASU) comprised of four complexes, which in this space group is equivalent to the unit cell (Figure 3 and Table 1). This structure was refined to 1.69 Å (R_{work}/R_{free}: 0.20/0.23). The ASU exhibits pseudo-2-fold rotational symmetry about its center, with two complexes modeled with their protein−RNA interfaces facing toward each other, and each of the other two complexes rotated ∼90° to their corresponding pseudosymmetry mate positioned at the interface of the two central protein chains (Figure S2). A notable difference between this structure and the previously published RocA complex is the way in which the RNA oligonucleotide binds. In the crystal structure of the RocA complex, each nucleotide in the 10-mer oligonucleotide has electron density which is well-resolved, whereas in this structure, only 8 of the 10 nucleotides in each chain are well-resolved. When the crystal contacts and solvent channels in the **CMLD012824** structure are examined, there is not sufficient space to build two additional nucleotides at the 5′ end of the RNA strands. This suggests that RNA binding in the **CMLD012824** complex is shifted by two nucleotide positions in order to allow for packing into this crystal form. Thus, what was previously described as π-stacking between A7 and G8 of the oligonucleotide with Ring A and Ring B of RocA in that complex is assigned as π-stacking between A5 and G6 of the oligonucleotide with Ring A and Ring B of **CMLD012824** (Figure 4). The most notable difference between the pairs of pseudosymmetry mates is the ring-stacking interactions of the 5′ end of the RNA strands. Whereas in Chains X and Z, the A1 nucleobases from each strand interact, in chains W and Y the A1 nucleobases stack with the A2 nucleobases of the other RNA strand (Figure S3). Additionally, the loop containing Motif VI common to DEAD-box helicases (G363−G370) that directly interacts with the AMPPNP ligand is apparently positioned differently across some of the chains.[6] In chains A and C, these loops adopt very similar conformations to one another, consistent with the canonical ATP-bound conformation, while in chain B, the density for the loop is clearly resolved in an alternate conformation, notably for ATP-interacting residues R365 and F366, and in chain D the entire loop is poorly resolved (data not shown). We do not predict these differences to have any impact on **CMLD012824** binding, as each AMPPNP ligand is well resolved in nearly identical position when the chains are aligned, and thus the quaternary complex appears unaffected. Other minor differences between the chains include the extent to which the N- and C-terminal residues can be resolved, namely, there is clear electron density for chain A 29−406, chain B 26−400, chain C 29−406, and chain D 26−399. Otherwise, each quaternary complex overlays with the others with low root-mean-square deviation (RMSD) of 0.079−0.197 $Å^2$.

The positioning and binding mode of **CMLD012824** are nearly identical to that of RocA from the previously reported structure and are consistent with the predicted binding mode from our previously published modeling.[21,26] The binding pocket for **CMLD012824** is formed at the protein−RNA interface, with the ADR positioned between consecutive purine nucleobases of the kinked RNA strand and with the C-ring projecting into a pocket formed at the interface of two α-helices (Figure 4). The presence of polypurine RNA is essential to the formation of a binding pocket. FTMap, a computational mapping server that identifies binding "hot spots," or surfaces with a high propensity for ligand binding,

https://doi.org/10.1021/acsomega.4c09421
ACS Omega 2025, 10, 5795−5808

Table 1. Data Collection and Refinement Statistics[a]

	Human eIF4A1/AMPPNP/CMLD012824/poly(AG)$_5$ complex PDB: 9DTS
Beamline	NSLS-II 17-ID-1 (AMX), BNL
Wavelength	0.9201
Resolution range	36.51−1.69 (1.75−1.69)
Space group	P 1
Unit cell (*a*, *b*, *c*) (*α*, *β*, *γ*)	66.11, 87.314, 93.159, 95.222, 105.287, 108.353
Total reflections	597,134 (52,543)
Unique reflections	201,775 (19,049)
Multiplicity	3.0 (2.7)
Completeness (%)	96.00 (91.16)
Mean *I*/sigma (*I*)	5.59 (0.80)
Wilson *B*-factor	27.27
R-merge	0.09026 (1.177)
R-meas	0.1095 (1.454)
R-pim	0.06117 (0.8404)
CC1/2	0.993 (0.368)
CC*	0.998 (0.733)
Reflections used in refinement	201,334 (19,047)
R-work	0.2028 (0.3432)
R-free	0.2400 (0.3363)
CC (work)	0.943 (0.638)
CC (free)	0.924 (0.575)
Number of non-hydrogen atoms	14,030
Macromolecules	12,839
Ligands	472
Solvent	899
Protein residues	1503
RMS (bonds)	0.012
RMS (angles)	1.25
Ramachandran favored (%)	97.73
Ramachandran allowed (%)	1.87
Ramachandran outliers (%)	0.40
Rotamer outliers (%)	1.27
Clashscore	8.58
Average *B*-factor	40.02
Macromolecules	39.95
Ligands	28.70
Solvent	41.81

[a]Statistics for the highest-resolution shell are given in parentheses.

did not identify the rocaglate binding site as a hot spot in the absence of the RNA, despite identifying the ATP-binding site and portions of the RNA binding sites.[31] As in the case of RocA, aryl rings A, B, and C (Figures 1A and 2) stack with A5, G6, and the side chain phenyl ring of F163, respectively, at distances between 3.6 and 4.0 Å (Figure 4). Unique to ADRs, the imidazoline N−H is engaged in a hydrogen bond to *N7* of G6. The distance and positioning of this hydrogen bond are comparable to that observed between the C8b tertiary hydroxyl of RocA and *N7* of G8 (2.7−2.9 Å, depending on the chain), which is thought to contribute to the unique purine selectivity of rocaglate binding.[26] In the present structure, the B ring methoxy group and N167 are within hydrogen bonding distance, which is not the case in the previously reported structure of RocA, due to a conformational difference in the N167 side chain (Figure 4). This is the first crystallographic observation of the formation of a hydrogen bond at this position and reaffirms the importance of a hydrogen bond acceptor at the *para*-position of the B ring of rocaglates for the potency of these compounds.[32] Hydrogen-bonding interactions provide a decrease in free energy that is offset by desolvation penalties; the high degree of solvent exposure at this site suggests that any gains to binding affinity imparted by this newly observed H-bond would be modest at best. Thus, we do not expect this interaction to fully explain the improved RNA-clamping activity observed for **CMLD012824**. Moreover, the position of the B ring does not differ between RocA and **CMLD012824**, so it is reasonable to assume that this hydrogen bond could also be made between eIF4A1 and RocA with a slight conformational adjustment of the protein. Given the considerable similarity between the binding interactions observed between the protein and each of the compounds, we next sought to use computational modeling to rationalize the substantial gains in the RNA-clamping and translation inhibition activity of ADRs over traditional rocaglates.

Computational Modeling of Rocaglate Ligands. In prior studies, we briefly described efforts to model **CMLD012824** into the published RocA X-ray structure using a manual overlay.[26] To leverage our new structural data and improve upon this earlier modeling, we performed computational docking (Glide, Schrodinger LLC) of **CMLD012824** and RocA into their respective X-ray structures.[33,34] The purpose of this docking was to determine whether the docking scores, which serve to approximate the predicted free energy of binding ($\Delta G_{binding}$), would reveal any meaningful differences between **CMLD012824** and RocA ligands. For both compounds, the top computationally predicted poses were in good agreement with the experimentally determined binding modes (Figure 5). In the case of **CMLD012824**, however, the *N*,*O*-dimethylhydroxylamine moiety of the *C*2-tethered Weinreb amide was predicted to be flipped approximately 180° relative to the experimentally determined pose (Figure 5B); given the lack of protein or RNA interactions and solvent exposure of these atoms, we consider this difference to have a negligible impact on binding energy. The Glide G_{scores} for **CMLD012824** and RocA docked into their native X-ray structures were quite similar (−11.1 *vs* −11.8 kcal/mol, respectively), and while the score for RocA was slightly improved relative to **CMLD012824**, limitations in the predictive accuracy of Glide docking (RMSD 2.3 kcal/mol) preclude a meaningful head-to-head comparison of these energies.[33] As such, these docking results support our empirical observations that RocA and **CMLD012824** each engage eIF4A/RNA in a highly similar manner with analogous binding interactions that are not expected to lead to substantial enthalpic differences in binding affinity.

Given these observations, we hypothesized that the conformational constraints imposed by the fused amidine ring may contribute to improved target engagement *via* conformational preorganization in a "binding-competent" mode, leading to reduced entropic penalties on binding. Conformational restriction by way of bond desaturation, ring formation, or other rigidification strategies such as intramolecular hydrogen bonding is a commonly deployed medicinal chemistry and structure-based drug design strategy to enhance compound potency by way of reducing the entropic term ($T\Delta S$) which offsets enthalpic gains (ΔH) achieved by ligand−target interactions.[35−42] We noted that the **CMLD012824** amidine N−H moiety in our X-ray crystal

https://doi.org/10.1021/acsomega.4c09421
ACS Omega 2025, 10, 5795−5808

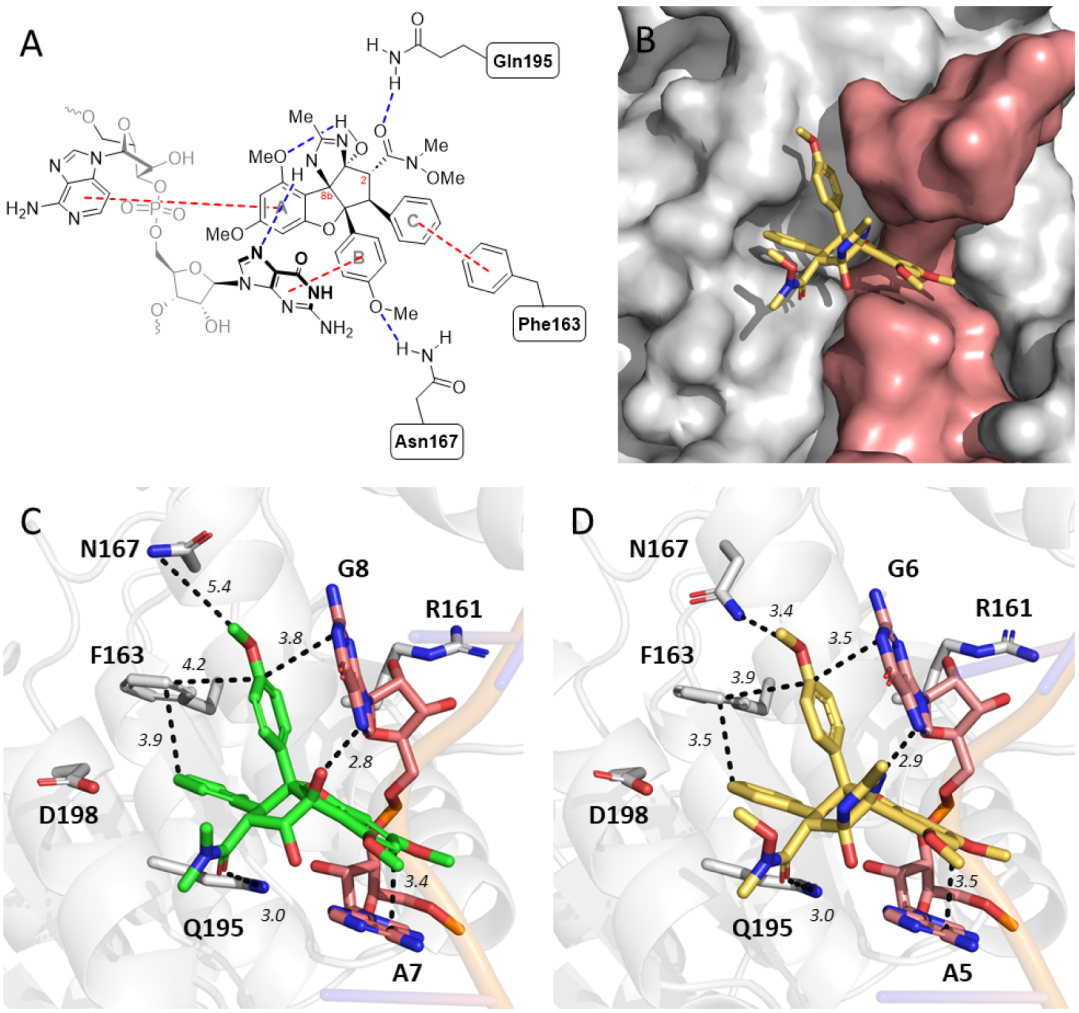

Figure 4. Binding pocket of **CMLD012824** and key amino-acid side-chain interactions. (A) Interaction diagram for bound eIF4A1−poly(AG)$_5$−**CMLD012824**. (B) Surface representation of the interface of eIF4A1 (white) and RNA (salmon) comprising the binding pocket for **CMLD012824** (yellow stick). Key interactions for RocA (C) and **CMLD012824** (D), with hydrogen bonds and hydrophobic interactions as dashed lines with lengths in Å. eIF4A1, off-white; poly(AG)$_5$, salmon; RocA, green; **CMLD012824**, yellow.

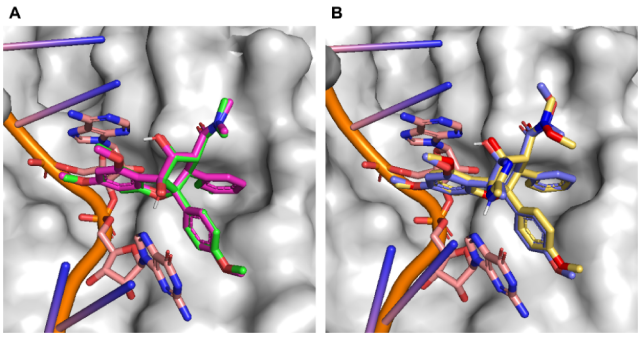

Figure 5. Computational docking of RocA and **CMLD012824** shows high agreement with the experimentally determined structures, without substantial differences in predicted binding energies. (A) Glide-predicted docking pose (G_{score}: −11.8 kcal/mol) for RocA (*magenta*) docked into the 5ZC9 eIF4A1:RNA structure (*white/salmon*) and overlaid with liganded RocA (*green*) from this structure. (B) Glide-predicted docking pose (G_{score}: −11.1 kcal/mol) for **CMLD012824** (*lavender*) docked into the eIF4A1−poly(AG)$_5$ structure (*white/salmon*) and overlaid with liganded **CMLD012824** from this structure (*gold*).

structure is in the same position as the RocA C8b hydroxyl, making a hydrogen bond to an RNA guanine base (G6/G8, respectively). In contrast to the untethered RocA hydroxyl, which can freely rotate to allow for competing hydrogen bonds with solvent (water) in the unbound state, the amidine N−H of **CMLD012824** is conformationally locked in the orientation required for hydrogen-bond donation. This observation led to the question of whether the rigidifying effect of the amidine fusion on the already-constrained cyclopenta[*b*]benzofuran rocaglate core may also impact the positioning of other key pendant functional groups with respect to their protein/RNA binding partners—namely, the Q195-interacting C2 substituent, the adenine-interacting A-ring, the guanine-interacting B-ring, and the Phe163-interacting C-ring. For example, during the development of rocaglate clinical candidate eFT226 (Zotatifin), Ernst and coworkers utilized DFT modeling of RocA to identify an optimal ∼40° torsion between the pendant "B" and "C" rocaglate rings that was deployed in synthetic candidate selection and was later recapitulated in the RocA X-ray crystal structure (PDB: 5ZC9).[43]

Computational docking programs such as Glide perform quite well at estimating the enthalpic contributions to ligand binding, but entropic effects are significantly more difficult to

https://doi.org/10.1021/acsomega.4c09421
ACS Omega 2025, 10, 5795−5808

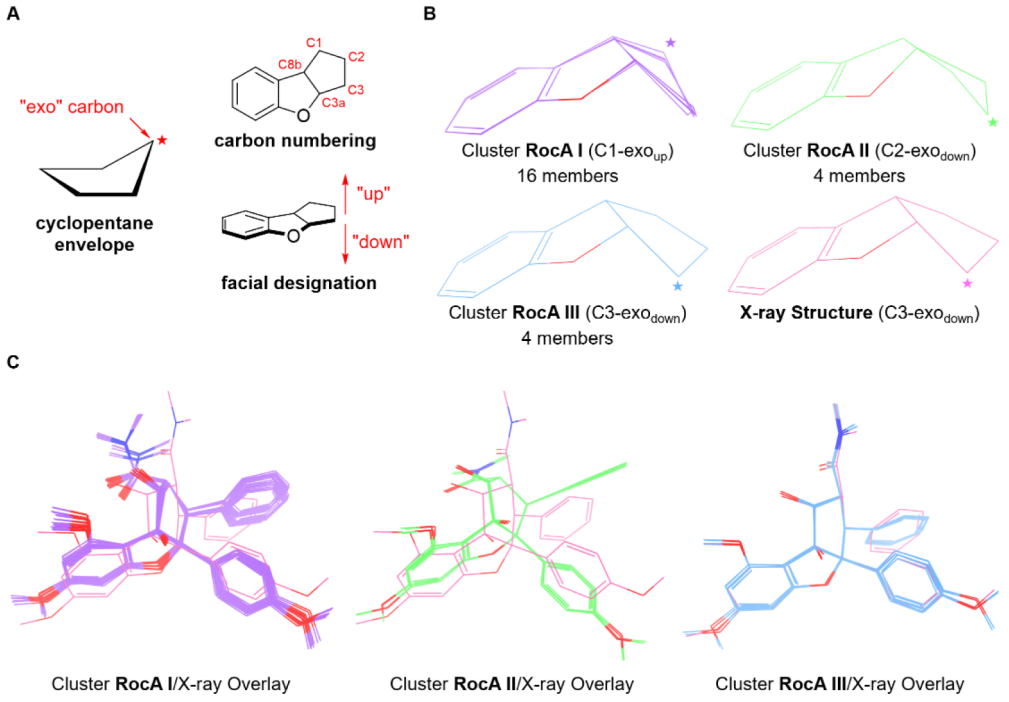

Figure 6. Conformational analysis of force-field computed RocA conformers. (A) Guide to nomenclature and numbering convention for cyclopenta[*b*]benzofuran core conformational classes based on the cyclopentane envelope conformation. (B) Overlays of each conformational cluster with only core atoms depicted, with the RocA X-ray bound core also depicted for comparison. For each depicted core conformation, the exo carbon is denoted with a star symbol. (C) All-atom overlays of each conformational cluster for RocA with eIF4A1-bound RocA from the X-ray structure (PDB: 5ZC9; *pink*).

capture due to the complex inherent molecular dynamics and the need to consider entropy changes in the protein and bulk solvent environment, in addition to changes in ligand entropy.[44−48] As such, entropic contributions are typically approximated in scoring functions at a low level of accuracy. For example, the standard precision Glide scoring function, which employs a modified version of the ChemScore scoring function, employs a rotatable bond term as an indirect approximation of the entropic penalties arising from the conformational restriction of the ligand.[33,49] More recent efforts to improve the precision of Glide scoring ("Glide XP" scoring) have attempted to address these concerns but have not achieved significant advancements in this area.[49] Importantly, since the fused cyclopenta[*b*]benzofuran ring system is entirely composed of "non-rotatable" bonds, we assume that any reduction in conformational entropy caused by further rigidification of this system would likely not be adequately captured by Glide's scoring functions. To better address this consideration, we instead sought to systematically examine and compare the conformational landscapes of **CMLD012824** and RocA to characterize how this apparent rigidification impacts the general eIF4A/RNA-binding pharmacophore of rocaglates.

We targeted a library of DFT-optimized conformers for each ligand using the established process of first deploying molecular mechanics to generate a library of unique low-energy conformers *via* fast and computationally inexpensive force field calculations, followed by more computationally intensive density functional theory (DFT) calculations on these conformers to arrive at more accurate minimized geometries and computed energies.[50] During the initial MacroModel conformational search stage, we noted a conspicuous absence of predicted RocA conformers in the eIF4A1−RNA-bound cyclopenta[*b*]benzofuran conformation when using the best-parametrized force fields (OPLS4 and OPLS_2005).[51−53] For both force fields, the closest all-atom RMSD from the bound conformation found among the conformational search output was >1.3 Å. This outcome was particularly concerning given prior computational studies on RocA, which identified a DFT-optimized lowest-energy conformer reported to have high conformational similarity to the X-ray liganded structure. Notably, force fields with lower quality parameters (MM3, MM2, AMBER, OPLS, MMFF, and MMFFs) all produced at least one conformer with RMSD < 0.3 Å compared to the X-ray bound conformation (Table S1).[43,54−57] To resolve this issue, the OPLS4 conformational search was repeated with a slightly extended energy window for retaining structures, increasing the 21.0 kJ/mol (5.02 kcal/mol) cutoff to 25.0 kJ/mol (5.97 kcal/mol), in line with recommendations by Sharapa and coworkers.[58] This resulted in a library of 24 unique RocA conformers, four of which closely resembled the X-ray bound RocA ligand (heavy-atom RMSD ≤ 1 Å).

Examination of the cyclopenta[*b*]benzofuran ring system conformation in each of the RocA conformers revealed that the benzofuran moiety is predominantly planar/flat, and that core differences are driven by pseudorotation of the fused cyclopentane ring (Figure 6A). The conformers were subclassified based on their cyclopentane envelope (or slightly twisted envelope) conformations, using a classification system wherein a different cyclopentane ring carbon assumes the "exo" position, pointed either above ("up") or below ("down") the plane of the benzofuran ring (according to the perspective depicted in Figure 6A). Three core conformational clusters were identified for RocA (Figures 6B and S4). The first cluster, which we named **RocA I**, comprised the 16 lowest-energy

https://doi.org/10.1021/acsomega.4c09421
ACS Omega 2025, 10, 5795−5808

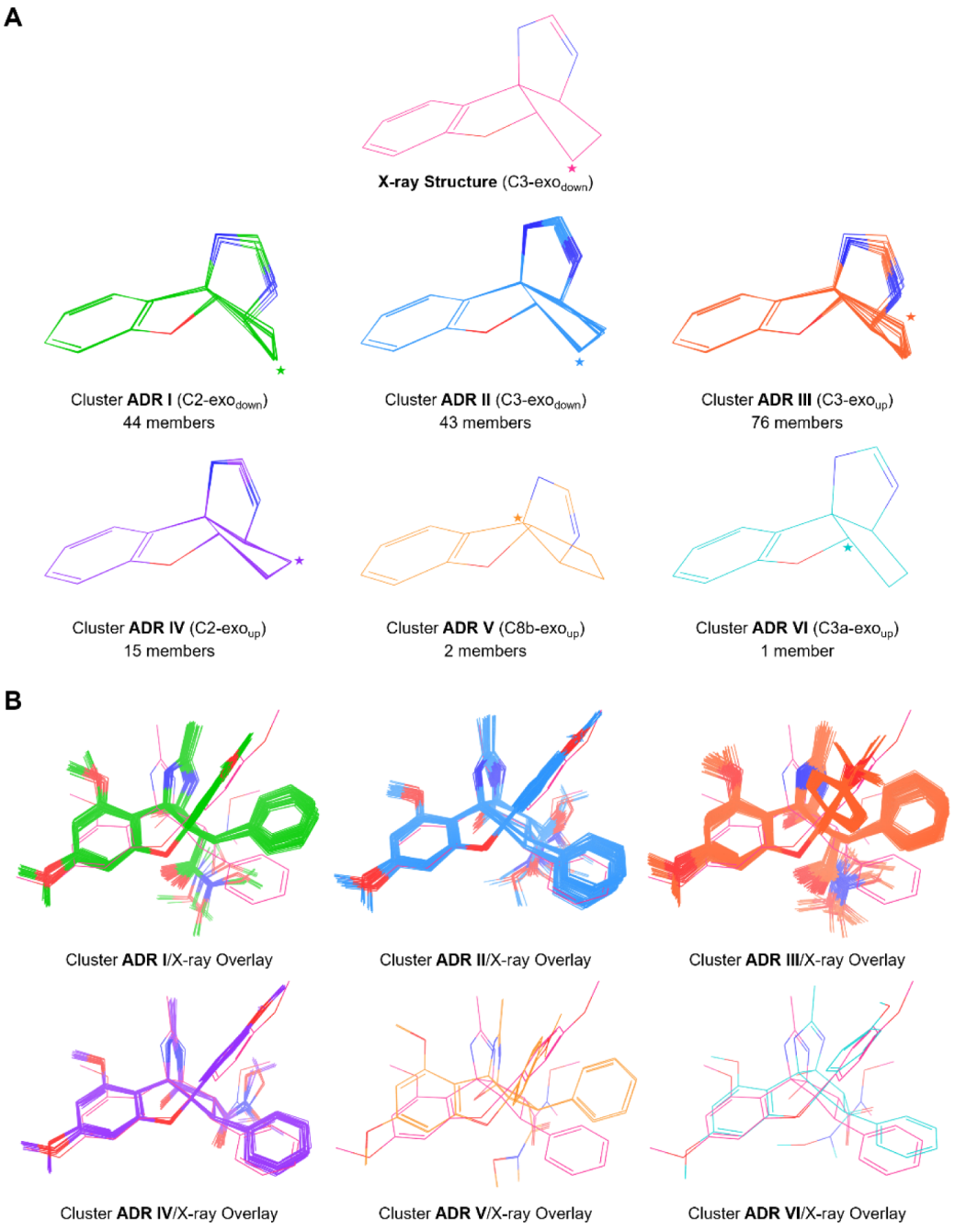

Figure 7. Conformational analysis of force-field computed **CMLD012824** conformers. (A) Overlays of each conformational cluster with only core atoms depicted, with the **CMLD012824** core from the liganded X-ray structure depicted for comparison. For each depicted core conformation, the exo carbon is denoted with a star symbol. (B) All-atom overlays of each conformational cluster for **CMLD012824**, aligned with eIF4A1-bound **CMLD012824** from the X-ray structure (*pink*).

conformers as predicted by force field calculations. In this core conformation, we observed the *C*1 carbon to adopt the *exo* position, positioned "up" relative to the benzofuran (C1-exo$_{up}$). A second cluster of four conformers, which showed a *C*2-exo$_{down}$ conformation, was assigned as **RocA II**. Lastly, the aforementioned subpopulation of four conformers binned as **RocA III** showed a cyclopentane envelope with the *C*3-exo$_{down}$ conformation, in excellent alignment with the bound RocA ligand from the published X-ray structure (PDB: 5ZC9, Figures 6C, S4, and S5), but were predicted by force-field calculations to be significantly higher in energy (+∼5.7 kcal/mol) than the lowest-energy **RocA I** conformer.

This MacroModel conformational search analysis was extended to ADR **CMLD012824**, again saving all unique conformers within a 25 kJ/mol (5.98 kcal/mol) energy window. This search produced 181 unique conformers that were similarly analyzed and subdivided into six unique core conformational clusters (Figures 7A, S6, and S7). Cluster **ADR I** contained 44 unique conformers, each of which had a *C*2-exo$_{down}$ conformation (analogous to cluster **RocA II**). Cluster **ADR II**, initially populated by 43 unique conformers, showed the same *C*3-exo$_{down}$ conformation observed in the complexed RocA/**CMLD012824** structures (Figure 7), and it was conformationally analogous to **RocA III**. Cluster **ADR III**

https://doi.org/10.1021/acsomega.4c09421
ACS Omega 2025, 10, 5795−5808

(*C*3-exo$_{up}$) contained 76 members and represents cyclopentane ring inversion from cluster **ADR II**. Cluster **ADR IV** (*C*2-exo$_{up}$), which contained 15 members, showed the second-lowest average RMSD to eIF4A1-complexed **CMLD012824**, but with a slight pseudorotation of the twisted envelope. Lastly, three additional high-energy conformers were assigned to clusters **ADR V** and **ADR VI**, with unique envelope conformations placing the *C*8b and *C*3a ring fusion carbons at the exo position, respectively (*C*8b-exo$_{up}$ and *C*3a-exo$_{up}$). Of note, no ADRs adopted the *C*1-exo$_{up}$ conformation that predominated the RocA conformer library (cluster **RocA I**), likely due to the conformational strain imposed by the imidazoline ring fusion at *C*1 blocking the required pseudorotation.

We next applied density functional theory (DFT) calculations to further refine the geometry of each conformer and to understand how the energetics of each conformational subpopulation compare to one another at a higher level of computational accuracy. Each conformer was geometrically optimized in Jaguar using B3LYP-D3/6-31g**, followed by single-point energy calculations using M06-2X/6-31g++** to predict relative gas phase energies.[59,60] For both ligands, the geometry optimizations slightly altered the distribution of conformers across their established subpopulations (Tables S2 and S3) and also led to the identification of one new sparsely populated, high-energy core cluster for each ligand (Figures S8−S11). Specifically, in the case of RocA, a new high-energy subpopulation (**RocA IV**, Figures S8 and S9) with four members was identified with a C8b-exo$_{down}$ conformation that, while distinct from cluster **RocA III**, more closely mimicked the bound conformation and projection of the B- and C-aromatic rings than clusters **RocA I** and **RocA II** (Figure S9). For **CMLD012824**, three high-energy conformers (relative energies ≥+11.7 kcal/mol) converged on a new geometry (**ADR VII**) with a C3a-exo$_{down}$ conformation (Figures S10 and S11).

To better visualize the energy landscape of the DFT-optimized conformer libraries, we plotted the heavy-atom RMSD from each conformer's respective crystallographically determined ligand conformation against its relative M06-2X/6-31g++** gas-phase energy (Figure 8). The analysis primarily focused on the conformers within a relative gas-phase energy window of 0−2 kcal/mol (Figure 8A,B, dashed gray line) based on the expectation that conformations with relative energies >2 kcal/mol from the lowest-energy conformer are not expected to be substantially populated.[61−64] Nonetheless, for **CMLD012824** (Figure 8A), we noted that a wider energy range (spanning from 0 to +3.5 kcal/mol) was exclusively populated with core conformation **ADR II**, the conformation with the highest similarity to the X-ray structure of bound **CMLD012824**. Further, all members of cluster **ADR II** showed a heavy-atom RMSD < 1.5 Å from that of the X-ray structure of the bound ligand, with higher RMSDs (>1.0 Å, ascribable to various rotamers of the C2-tethered Weinreb amide) generally correlating with higher computed energies. Together, these observations strongly support the premise that **CMLD012824** predominantly exists in a conformational state that is inherently preorganized to clamp eIF4A1 onto RNA.

Extending a similar analysis to RocA (Figure 8B) we found that, in contrast to **CMLD012824**, two distinct clusters (**RocA II** and **RocA III**) sat within the 0−2 kcal/mol energy window. Based on force-field-derived energies, we had considered the possibility that class **RocA III**, which most resembles the

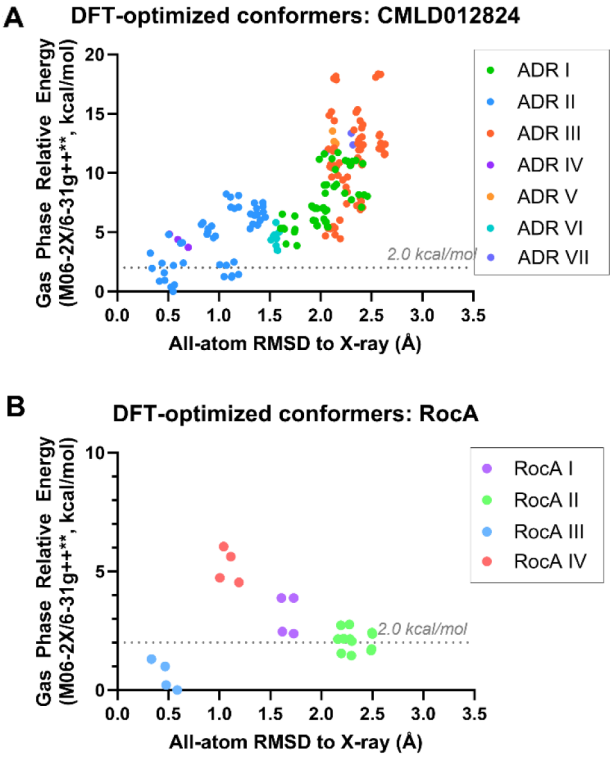

Figure 8. Energetic landscape of **CMLD012824**/RocA conformer classes. (A) Scatter plot of the heavy atom RMSD (in Å) from the **CMLD012824** X-ray structure *vs* the DFT-computed gas phase relative energy (M06-2X/6-31g++**, in kcal/mol) for each unique geometry-optimized **CMLD012824** conformer. Data points are colored according to the conformational cluster. Gray dashed line indicates the upper boundary of the 2.0 kcal/mol energy window for substantially populated conformational states at room temperature. (B) Scatter plot of the heavy-atom RMSD (in Å) from the RocA X-ray structure *vs* the DFT-computed gas phase relative energy (M06-2X/6-31g++**, in kcal/mol) for each unique geometry-optimized RocA conformer. Data points are colored according to conformational cluster, with the gray dashed line defined as in (A).

eIF4A1−RNA-bound ligand (all RMSDs ∼ 0.5 Å), represented a highly strained conformation. However, this turned out not to be the case, as this cluster was determined by DFT to be the lowest energy conformer class. This outcome is both consistent with prior findings in Zotatifin development and is perhaps unsurprising due to the known poor correlation between force field and DFT-derived energies.[43,62] The second lowest-energy cluster, **RocA II**, shows a significant conformational deviation from the X-ray bound conformation (all RMSDs > 2 Å). Although cluster **RocA II** is slightly higher in computed energy than cluster **RocA III**, we cannot exclude the possibility that clusters **RocA III** and **RocA II** are degenerate, given the inherent ∼2 kcal/mol accuracy limits of DFT.[63,65] Importantly, cluster **RocA II**, which bears a C2-exo$_{down}$ conformation that was not observed for any ADR, represents a reasonably populated low-energy core conformational state that would be disallowed upon binding of eIF4A1−RNA. It is also worth noting that a third cluster (**RocA I**) was also found in the expanded energy window of 2−3.5 kcal/mol. While the computed relative energies suggest that this conformation may not be populated to a significant extent at room temperature, the presence of a third conformational cluster within the same energy window that was exclusively populated

https://doi.org/10.1021/acsomega.4c09421
ACS Omega 2025, 10, 5795−5808

with the preorganized (**ADR II**) conformation of **CMLD012824** further underscores the conformational plasticity of the RocA core relative to the more rigidified ADR.

Collectively, these calculations strongly support our hypothesis that the fused amidine ring imparts significant conformational rigidification of the ADR scaffold, thereby locking the core in a productive conformation for eIF4A1−RNA binding. This includes the fused amidine N−H as a rigidified H-bond donor for target engagement of a guanine RNA base. This preorganization ensures that **CMLD012824** likely engages eIF4A1 and RNA without experiencing a significant loss in entropy upon binding, contrasting with more conformationally flexible, nonamidino rocaglate ligands such as RocA. This phenomenon likely contributes to the observed enhanced RNA clamping ability and translation inhibition potency of ADR **CMLD012824** relative to non-amidino rocaglates.

CONCLUSIONS

In the last several years, rocaglates have emerged as a class of compounds of considerable interest in drug discovery, possessing the unique quality of sequence-selective translation repression as small molecules. Much more work needs to be done to expand our understanding of these compounds in the interest of developing them into the potent anticancer and anti-infectious agents they have the potential to be. The present investigation represents an important step in that direction, with the determination of just the third such X-ray crystal structure of a rocaglate bound to eIF4A1, and the first of an amidino-rocaglate, **CMLD012824**, for which the binding mode had only previously been predicted computationally. By comparison to the previous structure, we were able to identify the conserved interactions of rocaglates and ADRs with their cognate RNA and eIF4A1. Our computational docking experiments supported the structural observations that suggest that RocA and **CMLD012824** both engage RNA in a similar way and have similar enthalpic gains upon binding, prompting an investigation of the entropic determinants of binding for each of these compounds. DFT-optimized computational modeling illustrated a difference in the distributions of conformers of RocA and **CMLD012824**. Gas-phase energy calculations of these different conformer subpopulations were categorized into subpopulations for RocA and **CMLD012824**, with the ADR having a single subpopulation within an ∼2 kcal/mol window of the experimentally determined conformer from the X-ray structure, while RocA existed in two unique conformers within this window, suggesting that the ADR, due to the presence of the unique amidine ring fusion on the rocaglate scaffold, was inherently preorganized in a conformation capable of clamping eIF4A1 onto purine RNA. This study illustrates how the rigidifying effect of the ADR amadine ring fusion can be used to improve potency for development as potential antineoplastic, antiviral, and antiparasitic drugs.

EXPERIMENTAL SECTION

Construct Design and Protein Expression. A sequence encoding residues 21−406 of eIF4A1 with codons optimized for expression in *E. coli* (Twist BioScience) was cloned using Gibson Assembly into a pTB146 vector to include an N-terminal 6× histidine tag followed by a Small Ubiquitin-like Modifier (SUMO) tag. The truncation of the first 20 amino acids of eIF4A1 was based on the lack of electron density for these residues in the previously published structure of eIF4A1:RocA (5ZC9). The resulting pTB146-His$_6$-SUMO-eIF4A1(21−406) was transformed into BL21(DE3) cells (New England Biolabs), plated, and incubated overnight. Single colonies were isolated and used to inoculate small "starter" cultures of Luria Broth containing 100 μg/mL carbenicillin and grown overnight for ca. 12−15 h at 37 °C. These cultures were used to inoculate large-scale growths, grown at 37 °C until OD_{600} = 0.6−0.8. Protein expression was induced with IPTG added to a final concentration of 1 mM. Flasks were incubated overnight for about 18 h at 16 °C, whereupon cells were harvested by centrifugation at 4000*g* for 10 min. The cell pellet was stored at −80 °C.

Protein Purification. eIF4A1(21−406) was purified as previously described with the following modifications.[66] Clarified lysate was applied to HisPur Ni-NTA Resin (Thermo Scientific) in a gravity column instead of using FPLC. Protein was eluted in a single step using 20 mL of a buffer containing 262.5 mM imidazole. Eluted protein was dialyzed overnight together with SUMO Protease into a buffer lacking imidazole to cleave purification tags followed by subtractive IMAC (SUMO Protease prepped in-house according to a published protocol).[67] Size-exclusion chromatography (SEC) on a 26 mm × 600 mm HiPrep 26/60 Sephacryl S-300 HR column (Cytiva), equilibrated in 50 mM EPPS-KOH pH 8.0, 100 mM KCl, 5 mM $MgCl_2$, 1 mM DTT, and 0.1 mM EDTA, was used to achieve a homogeneity (evaluated by SDS-PAGE and >80% monodispersity in dynamic light scattering) sufficient for crystallization experiments. Amicon Ultra centrifugal filter devices (30 kDa cutoff) were used to concentrate the protein before and after SEC. SEC-purified fractions were concentrated to between 8 and 15 mg/mL, whereupon glycerol was added to a final glycerol concentration of 10%, and aliquots were flash-frozen in liquid nitrogen and stored at −80 °C.

Chemical Synthesis. The chiral, enantioenriched ADR **CMLD012824** was synthesized by the condensation of a rocaglate enol tosylate precursor (>99% e.e.) with methyl amidine according to our literature procedure.[25] The compound employed in this study possessed >95% purity as determined by UPLC-MS-ELSD analysis.

Crystallization. Purified eIF4A1(21−406) (5−15 mg/mL) was mixed with superstoichiometric (1.5×) amounts of **CMLD012824**, nonhydrolyzable ATP-analog AMPPNP (5×), and poly(AG)$_5$ RNA (3×). AMPPNP (MilliporeSigma) and poly(AG)$_5$ RNA (Horizon Discovery/Dharmacon) were purchased commercially. A protein cocktail was mixed with a well solution in various proportions to yield a protein concentration of 10 mg/mL after equilibration. Vapor diffusion with sitting-drop geometry at 17 °C was utilized. Initial cubic crystals, smaller than 25 μm, were identified from a sparse matrix screen (Hampton Research PEG/Ion) in a condition comprised of 0.2 M ammonium acetate and 20% w/v PEG 3350. Crystal optimization strategies included improving protein purification quality through a more stringent selection of purified fractions and varying the precipitant polymer. The final condition comprised 0.2 M ammonium acetate and 8% PEG20000 and 10% Hampton Silver Bullet Reagent B5, a crystallization additive cocktail comprised of 0.33% w/v 2,7-naphthalenedisulfonic acid disodium salt, 0.33% w/v azelaic acid, 0.33% w/v *trans*-cinnamic acid, and 0.02 M HEPES sodium pH 6.8. *N.B.* The crystal used to collect the final data set was grown from a condition including the Hampton Silver Bullet Reagent B5; however, several crystals were harvested

https://doi.org/10.1021/acsomega.4c09421
ACS Omega 2025, 10, 5795−5808

from wells containing other Silver Bullet additives and diffracted to similar resolution in the same space group. It does not appear that the Silver Bullets altered the crystallization or diffraction characteristics in this experiment.

Data Collection and Structure Refinement. Crystal harvesting/cryoprotection solutions were prepared by reproducing the well condition with the addition of 10% glycerol. Crystals were harvested from the mother liquor and incubated in the cryoprotection solution for 0.5−3 min prior to flash-cooling in liquid nitrogen at 100 K. X-ray diffraction data was collected at the Brookhaven National Laboratory at the National Synchrotron Light Source II (Upton, NY) on beamline 17-ID-1 (AMX) outfitted with an Eiger 9M detector. Diffraction data were collected under nitrogen gas cooled to 100 K and were processed, integrated, and scaled using XDS.[68] Initial phases were calculated using the previously determined structure of eIF4A1 in complex with RocA, poly(AG)$_5$, and AMPPNP (PDB: 5ZC9) with small molecule ligands and waters removed as a search model for molecular replacement in PHENIX Phaser-MR.[69] Multiple rounds of refinement in PHENIX Refine using individual B-factors, TLS parameters, and addition of waters, along with manual model building, were used in iterative rounds.[70] Ligands were positioned in electron density manually using Coot and validated using Fo−Fc omit and Polder electron density maps in PHENIX.[71] All images were generated in PyMOL.[72]

Computational Docking. RocA and **CMLD012824** ligands were prepared for docking using the LigPrep application in the Maestro software environment (Version 2024-2, Schrödinger LLC). Likewise, eIF4A1/RNA receptor structures were prepared from the 5ZC9 X-ray structure and the ADR-bound X-ray structure reported herein using the default Protein Preparation Workflow in Maestro. The protein preparation protocol involved structure preprocessing, hydrogen-bond optimization, and restrained minimization (S-OPLS force field, hydrogen atoms freely minimized and heavy atoms minimized to RMSD 0.3 Å, and removal of water >5 Å from heavy atoms). Docking grids were then generated from the prepared structures, sized and centered at the existing rocaglate/ADR ligand. Glide docking of each ligand into its respective receptor grid was then performed using default settings at standard precision (SP), with five output poses produced per ligand. The top-scored pose (Glide G_{scores}) for each compound was selected for analysis.

MacroModel Conformational Searches. Conformer libraries for RocA and **CMLD012824** were generated using the MacroModel Conformational Search tool (force field: OPLS4, method: torsional sampling/MCMM, solvent: water, torsional sampling: enhanced, energy window for saving structure: 25 kJ/mol) in the Maestro software environment (Version 2024-2, Schrödinger LLC). Conformer libraries were manually inspected to remove redundant conformers and binned according to core conformation with the aid of comparative overlays and RMSD calculation (either all-atom or select atom) by using the "Superposition" tool in Maestro. Relative potential energies were calculated by subtracting the potential energy of each library member from the potential energy of the lowest-energy conformer in that library (for which the relative potential energy was 0 kJ/mol).

Jaguar DFT Calculations. The output conformer libraries for the MacroModel conformational search were subjected to DFT geometry optimizations in the gas phase using the Jaguar application in the Maestro software environment (Version 2024-2, Schrödinger LLC). Optimizations were performed at the B3LYP-D3 level of theory with the 6-31g** basis set. Each geometry-optimized structure was then subjected to single point energy conformations using Jaguar at the MO6-2X level of theory with the 6-31g++** basis set. The total number of canonical orbitals employed was 831 for RocA and 910 for **CMLD012824**. A heavy atom RMSD from the respective X-ray bound ligand for each conformer was calculated using the Superposition tool in the Maestro software environment. Scatter plots of heavy atom RMSD *versus* relative potential energy for all conformers were generated in Prism (Version 10.2.3, GraphPad, Inc.).

■ ASSOCIATED CONTENT

Supporting Information

The Supporting Information is available free of charge at https://pubs.acs.org/doi/10.1021/acsomega.4c09421.

Structures of rocaglate derivatives, ribbon diagrams of the eIF4A1−RNA−**CMLD012824**−AMPPNP asymmetric unit, force field conformations for RocA and **CMLD012824**, DFT-optimized conformations for RocA and **CMLD012824**, tables of computational results, coordinates and gas phase energies for the lowest-energy members of conformational clusters of RocA and **CMLD012824**, and supplementary references (PDF)

■ AUTHOR INFORMATION

Corresponding Authors

John A. Porco, Jr − *Department of Chemistry, Boston University, Boston, Massachusetts 02215, United States;* orcid.org/0000-0002-2991-5680; Email: porco@bu.edu

Karen N. Allen − *Department of Pharmacology, Physiology & Biophysics and Department of Chemistry, Boston University, Boston, Massachusetts 02215, United States;* orcid.org/0000-0001-7296-0551; Email: drkallen@bu.edu

Authors

James F. Conley − *Department of Pharmacology, Physiology & Biophysics, Boston University, Boston, Massachusetts 02215, United States;* orcid.org/0000-0002-1366-4231

Lauren E. Brown − *Department of Chemistry, Boston University, Boston, Massachusetts 02215, United States;* orcid.org/0000-0001-9489-484X

James H. McNeely − *Department of Chemistry, Boston University, Boston, Massachusetts 02215, United States;* orcid.org/0000-0001-6763-0531

[⊥]**Jerry Pelletier** − *Department of Biochemistry, McGill University, Montreal, Quebec H3G 1Y6, Canada;* orcid.org/0000-0003-1963-6466

Complete contact information is available at: https://pubs.acs.org/10.1021/acsomega.4c09421

Notes

The authors declare no competing financial interest.

[⊥]Deceased 9/17/23.

■ ACKNOWLEDGMENTS

We thank the National Institutes of Health (NIH) (R35 GM118173 and U01 TR002625) for financial support. This research used the facilities of the AMX beamline of the National Synchrotron Light Source II, a U.S. Department of Energy (DOE) Office of Science User Facility operated for the

https://doi.org/10.1021/acsomega.4c09421
ACS Omega 2025, 10, 5795−5808

DOE Office of Science by Brookhaven National Laboratory under Contract No. DE-SC0012704. The Center for BioMolecular Structure (CBMS) is primarily supported by the National Institutes of Health, National Institute of General Medical Sciences (NIGMS) through a Center Core P30 Grant (P30GM133893), and by the DOE Office of Biological and Environmental Research (KP1605010).

■ ABBREVIATIONS

eIF4A1, eukaryotic initiation factor 4A-1; RocA, rocaglamide A; ADR, amidino-rocaglate; DFT, density functional theory; m7G, 5′-7-methylguanosine; eIF, eukaryotic initiation factor; 5′-UTR, 5′-untranslated region; SUMO, small ubiquitin-like modifier; SEC, size exclusion chromatography; LEC, lowest-energy conformer

■ REFERENCES

(1) Jackson, R. J.; Hellen, C. U. T.; Pestova, T. V. The Mechanism of Eukaryotic Translation Initiation and Principles of Its Regulation. *Nat. Rev. Mol. Cell Biol.* **2010**, *11*, 113−127.
(2) Lu, W. T.; Wilczynska, A.; Smith, E.; Bushell, M. The Diverse Roles of the EIF4A Family: You Are the Company You Keep. *Biochem. Soc. Trans.* **2014**, *42* (1), 166−172.
(3) Yoder-Hill, J.; Pause, A.; Sonenberg, N.; Merrick, W. C. The P46 Subunit of Eukaryotic Initiation Factor (EIF)-4F Exchanges with EIF-4A. *J. Biol. Chem.* **1993**, *268* (8), 5566−5573.
(4) Williams-Hill, D. M.; Duncan, R. F.; Nielsen, P. J.; Tahara, S. M. Differential Expression of the Murine Eukaryotic Translation Initiation Factor Isogenes EIF4A(I) and EIF4A(II) Is Dependent upon Cellular Growth Status. *Arch. Biochem. Biophys.* **1997**, *338* (1), 111−120.
(5) Galicia-Vázquez, G.; Cencic, R.; Robert, F.; Agenor, A. Q.; Pelletier, J. A Cellular Response Linking EIF4AI Activity to EIF4AII Transcription. *RNA* **2012**, *18* (7), 1373−1384.
(6) Linder, P.; Jankowsky, E. From Unwinding to Clamping - the DEAD Box RNA Helicase Family. *Nat. Rev. Mol. Cell Biol.* **2011**, *12* (8), 505−516.
(7) Shah, P.; Ding, Y.; Niemczyk, M.; Kudla, G.; Plotkin, J. B. Rate-Limiting Steps in Yeast Protein Translation. *Cell* **2013**, *153* (7), 1589−1601.
(8) Raza, F.; Waldron, J. A.; Quesne, J. L. Translational Dysregulation in Cancer: EIF4A Isoforms and Sequence Determinants of EIF4A Dependence. *Biochem. Soc. Trans.* **2015**, *43* (6), 1227−1233.
(9) Kim, S.; Salim, A. A.; Swanson, S. M.; Kinghorn, A. D. Potential of Cyclopenta[b]Benzofurans from Aglaia Species in Cancer Chemotherapy. *Anticancer Agents Med. Chem.* **2008**, *6* (4), 319−345.
(10) Wolfe, A. L.; Singh, K.; Zhong, Y.; Drewe, P.; Rajasekhar, V. K.; Sanghvi, V. R.; Mavrakis, K. J.; Jiang, M.; Roderick, J. E.; Van der Meulen, J.; Schatz, J. H.; Rodrigo, C. M.; Zhao, C.; Rondou, P.; de Stanchina, E.; Teruya-Feldstein, J.; Kelliher, M. A.; Speleman, F.; Porco, J. A.; Pelletier, J.; Rätsch, G.; Wendel, H. G. RNA G-Quadruplexes Cause EIF4A-Dependent Oncogene Translation in Cancer. *Nature* **2014**, *513* (7516), 65−70.
(11) Chu, J.; Pelletier, J. Targeting the EIF4A RNA Helicase as an Anti-Neoplastic Approach. *Biochim. Biophys. Acta, Gene Regul. Mech.* **2015**, *1849* (7), 781−791.
(12) Heerma van Voss, M. R.; van Diest, P. J.; Raman, V. Targeting RNA Helicases in Cancer: The Translation Trap. *Biochim. Biophys. Acta, Rev. Cancer* **2017**, *1868* (2), 510−520.
(13) Ebada, S. S.; Lajkiewicz, N.; Porco, J. A.; Li-Weber, M.; Proksch, P. Chemistry and Biology of Rocaglamides (= Flavaglines) and Related Derivatives from Aglaia Species (Meliaceae), In *Progress in the Chemistry of Organic Natural Products*; Springer: Vienna, 2011, Vol. *94*, pp. 1−58. .
(14) Li-Weber, M. Molecular Mechanisms and Anti-Cancer Aspects of the Medicinal Phytochemicals Rocaglamides (=flavaglines). *Int. J. Cancer* **2015**, *137* (8), 1791−1799.
(15) Iwasaki, S.; Floor, S. N.; Ingolia, N. T. Rocaglates Convert DEAD-Box Protein EIF4A into a Sequence-Selective Translational Repressor. *Nature* **2016**, *534* (7608), 558−561.
(16) King, M. L.; Chiang, C. C.; Ling, H. C.; Fujita, E.; Ochiai, M.; McPhail, A. T. X-Ray Crystal Structure of Rocaglamide, a Novel Antileulemic 1H-Cyclopenta[b]Benzofuran from Aglaia Elliptifolia. *J. Chem. Soc., Chem. Commun.* **1982**, No. 20, 1150−1151.
(17) Zhao, Q.; Abou-Hamdan, H.; Désaubry, L. Recent Advances in the Synthesis of Flavaglines, a Family of Potent Bioactive Natural Compounds Originating from Traditional Chinese Medicine. *Eur. J. Org. Chem.* **2016**, *2016* (36), 5908−5916.
(18) Greger, H. Comparative Phytochemistry of Flavaglines (=Rocaglamides), a Group of Highly Bioactive Flavolignans from Aglaia Species (Meliaceae). *Phytochem. Rev.* **2022**, *21* (3), 725−764.
(19) Gerson-Gurwitz, A.; Young, N. P.; Goel, V. K.; Eam, B.; Stumpf, C. R.; Chen, J.; Fish, S.; Barrera, M.; Sung, E.; Staunton, J.; Chiang, G. G.; Webster, K. R.; Thompson, P. A. Zotatifin, an EIF4A-Selective Inhibitor, Blocks Tumor Growth in Receptor Tyrosine Kinase Driven Tumors. *Front. Oncol.* **2021**, *11*, 766298.
(20) Sharma, M.; Berz, D.; Caswell-Jin, J. L.; Spira, A. I.; Fulgar, G. A.; Densel, M.; Rana, N.; Sperry, S.; Warner, D.; Meric-Bernstam, F.; Group, A. A. Phase 1/2 Dose Expansion Study Evaluating First-in-Class EIF4A Inhibitor Zotatifin in Patients with ER+ Metastatic Breast Cancer. *J. Clin. Oncol.* **2023**, *41* (16), 1080.
(21) Iwasaki, S.; Iwasaki, W.; Takahashi, M.; Sakamoto, A.; Watanabe, C.; Shichino, Y.; Floor, S. N.; Fujiwara, K.; Mito, M.; Dodo, K.; et al. The Translation Inhibitor Rocaglamide Targets a Bimolecular Cavity between EIF4A and Polypurine RNA. *Mol. Cell* **2019**, *73* (4), 738−748.e9.
(22) Naineni, S. K.; Bhatt, G.; Jiramongkolsiri, E.; Robert, F.; Cencic, R.; Huang, S.; Nagar, B.; Pelletier, J. Protein−RNA Interactions Mediated by Silvestrol—Insight into a Unique Molecular Clamp. *Nucleic Acids Res.* **2024**, *52* (20), 12701−12711.
(23) Naineni, S. K.; Liang, J.; Hull, K.; Cencic, R.; Zhu, M.; Northcote, P.; Teesdale-Spittle, P.; Romo, D.; Nagar, B.; Pelletier, J. Functional Mimicry Revealed by the Crystal Structure of an EIF4A: RNA Complex Bound to the Interfacial Inhibitor, Desmethyl Pateamine A. *Cell Chem. Biol.* **2021**, *28*, 825−834.
(24) Saito, H.; Handa, Y.; Chen, M.; Schneider-Poetsch, T.; Shichino, Y.; Takahashi, M.; Romo, D.; Yoshida, M.; Fürstner, A.; Ito, T.; Fukuzawa, K.; Iwasaki, S. DMDA-PatA Mediates RNA Sequence-Selective Translation Repression by Anchoring EIF4A and DDX3 to GNG Motifs. *Nat. Commun.* **2024**, *15*, 1.
(25) Zhang, W.; Chu, J.; Cyr, A. M.; Yueh, H.; Brown, L. E.; Wang, T. T.; Pelletier, J.; Porco, J. A. Intercepted Retro-Nazarov Reaction: Syntheses of Amidino-Rocaglate Derivatives and Their Biological Evaluation as EIF4A Inhibitors. *J. Am. Chem. Soc.* **2019**, *141* (32), 12891−12900.
(26) Chu, J.; Zhang, W.; Cencic, R.; Devine, W. G.; Beglov, D.; Henkel, T.; Brown, L. E.; Vajda, S.; Porco, J. A., Jr; Pelletier, J. Amidino-Rocaglates: A Potent Class of EIF4A Inhibitors. *Cell Chem. Biol.* **2019**, *26* (11), 1586−1593.e3.
(27) Chu, J.; Zhang, W.; Cencic, R.; O'Connor, P. B. F.; Robert, F.; Devine, W. G.; Selznick, A.; Henkel, T.; Merrick, W. C.; Brown, L. E.; et al. Rocaglates Induce Gain-of-Function Alterations to EIF4A and EIF4F. *Cell Rep.* **2020**, *30*, 2481.
(28) Praditya, D. F.; Klöhn, M.; Brüggemann, Y.; Brown, L. E.; Porco, J. A.; Zhang, W.; Kinast, V.; Kirschning, A.; Vondran, F. W. R.; Todt, D.; Steinmann, E. Identification of Structurally Re-Engineered Rocaglates as Inhibitors against Hepatitis E Virus Replication. *Antiviral Res.* **2022**, *204*, 105359.
(29) Yount, R. G.; Babcock, D.; Ballantyne, W.; Ojala, D. Adenylyl Imidodiphosphate, an Adenosine Triphosphate Analog Containing a P-N-P Linkage. *Biochemistry* **1971**, *10* (13), 2484−2489.
(30) Lacabanne, D.; Wiegand, T.; Wili, N.; Kozlova, M. I.; Cadalbert, R.; Klose, D.; Mulkidjanian, A. Y.; Meier, B. H.;

https://doi.org/10.1021/acsomega.4c09421
ACS Omega 2025, 10, 5795−5808

Böckmann, A. ATP Analogues for Structural Investigations: Case Studies of a DnaB Helicase and an ABC Transporter. *Molecules* **2020**, *25*, 5268.
(31) Kozakov, D.; Grove, L. E.; Hall, D. R.; Bohnuud, T.; Mottarella, S.; Luo, L.; Xia, B.; Beglov, D.; Vajda, S. The FTMap Family of Web Servers for Determining and Characterizing Ligand Binding Hot Spots of Proteins HHS Public Access. *Nat. Protoc.* **2015**, *10* (5), 733−755.
(32) Thuaud, F.; Bernard, Y.; Turkeri, G.; Dirr, R.; Aubert, G.; Cresteil, T.; Baguet, A.; Tomasetto, C.; Svitkin, Y.; Sonenberg, N.; Nebigil, C. G.; Désaubry, L. Synthetic Analogue of Rocaglaol Displays a Potent and Selective Cytotoxicity in Cancer Cells: Involvement of Apoptosis Inducing Factor and Caspase-12. *J. Med. Chem.* **2009**, *52* (16), 5176−5187.
(33) Friesner, R. A.; Banks, J. L.; Murphy, R. B.; Halgren, T. A.; Klicic, J. J.; Mainz, D. T.; Repasky, M. P.; Knoll, E. H.; Shelley, M.; Perry, J. K.; Shaw, D. E.; Francis, P.; Shenkin, P. S. Glide: A New Approach for Rapid, Accurate Docking and Scoring. 1. Method and Assessment of Docking Accuracy. *J. Med. Chem.* **2004**, *47* (7), 1739−1749.
(34) Halgren, T. A.; Murphy, R. B.; Friesner, R. A.; Beard, H. S.; Frye, L. L.; Pollard, W. T.; Banks, J. L. Glide: A New Approach for Rapid, Accurate Docking and Scoring. 2. Enrichment Factors in Database Screening. *J. Med. Chem.* **2004**, *47* (7), 1750−1759.
(35) Gavuzzo, E.; Pochetti, G.; Mazza, F.; Gallina, C.; Gorini, B.; D'Alessio, S.; Pieper, M.; Tschesche, H.; Tucker, P. A. Two Crystal Structures of Human Neutrophil Collagenase, One Complexed with a Primed- and the Other with an Unprimed-Side Inhibitor: Implications for Drug Design. *J. Med. Chem.* **2000**, *43* (18), 3377−3385.
(36) Chimenti, F.; Maccioni, E.; Secci, D.; Bolasco, A.; Chimenti, P.; Granese, A.; Carradori, S.; Alcaro, S.; Ortuso, F.; Yáñez, M.; Orallo, F.; Cirilli, R.; Ferretti, R.; Torre, F. L. Synthesis, Stereochemical Identification, and Selective Inhibitory Activity against Human Monoamine Oxidase-B of 2-Methylcyclohexylidene-(4-arylthiazol-2-yl)hydrazones. *J. Med. Chem.* **2008**, *51* (16), 4874−4880.
(37) Kuhn, B.; Mohr, P.; Stahl, M. Intramolecular Hydrogen Bonding in Medicinal Chemistry. *J. Med. Chem.* **2010**, *53* (6), 2601−2611.
(38) Rühmann, E. H.; Rupp, M.; Betz, M.; Heine, A.; Klebe, G. Boosting Affinity by Correct Ligand Preorganization for the S2 Pocket of Thrombin: A Study by Isothermal Titration Calorimetry, Molecular Dynamics, and High-Resolution Crystal Structures. *ChemMedchem* **2016**, *11* (3), 309−319.
(39) Foloppe, N.; Chen, I. J. Towards Understanding the Unbound State of Drug Compounds: Implications for the Intramolecular Reorganization Energy upon Binding. *Bioorg. Med. Chem.* **2016**, *24* (10), 2159−2189.
(40) Scott, J. S.; Degorce, S. L.; Anjum, R.; Culshaw, J.; Davies, R. D. M.; Davies, N. L.; Dillman, K. S.; Dowling, J. E.; Drew, L.; Ferguson, A. D.; Groombridge, S. D.; Halsall, C. T.; Hudson, J. A.; Lamont, S.; Lindsay, N. A.; Marden, S. K.; Mayo, M. F.; Pease, J. E.; Perkins, D. R.; Pink, J. H.; Robb, G. R.; Rosen, A.; Shen, M.; McWhirter, C.; Wu, D. Discovery and Optimization of Pyrrolopyrimidine Inhibitors of Interleukin-1 Receptor Associated Kinase 4 (IRAK4) for the Treatment of Mutant MYD88 L265P Diffuse Large B-Cell Lymphoma. *J. Med. Chem.* **2017**, *60* (24), 10071−10091.
(41) Fang, Z.; Song, Y.; Zhan, P.; Zhang, Q.; Liu, X. Conformational Restriction: An Effective Tactic in'Follow-on'-Based Drug Discovery. *Future Med. Chem.* **2014**, *6* (8), 885−901.
(42) Finch, H. The Conformational Musings of a Medicinal Chemist. *Drug Discov. Today* **2014**, *19* (3), 320−325.
(43) Ernst, J. T.; Thompson, P. A.; Nilewski, C.; Sprengeler, P. A.; Sperry, S.; Packard, G.; Michels, T.; Xiang, A.; Tran, C.; Wegerski, C. J.; Eam, B.; Young, N. P.; Fish, S.; Chen, J.; Howard, H.; Staunton, J.; Molter, J.; Clarine, J.; Nevarez, A.; Chiang, G. G.; Appleman, J. R.; Webster, K. R.; Reich, S. H. Design of Development Candidate EFT226, a First in Class Inhibitor of Eukaryotic Initiation Factor 4A RNA Helicase. *J. Med. Chem.* **2020**, *63* (11), 5879−5955.
(44) Ajay; Murcko, M. A. Computational Methods to Predict Binding Free Energy in Ligand-Receptor Complexes. *J. Med. Chem.* **1995**, *38* (26), 4953−4967.
(45) Chang, C. E. A.; Chen, W.; Gilson, M. K. Ligand Configurational Entropy and Protein Binding. *Proc. Natl. Acad. Sci. U. S. A.* **2007**, *104* (5), 1534−1539.
(46) Duan, L.; Liu, X.; Zhang, J. Z. H. Interaction Entropy: A New Paradigm for Highly Efficient and Reliable Computation of Protein-Ligand Binding Free Energy. *J. Am. Chem. Soc.* **2016**, *138* (17), 5722−5728.
(47) Pantsar, T.; Poso, A. Binding Affinity via Docking: Fact and Fiction. *Molecules* **2018**, *23* (8), 1899.
(48) Winkler, D. A. Ligand Entropy Is Hard but Should Not Be Ignored. *J. Chem. Inf. Model* **2020**, *60* (10), 4421−4423.
(49) Friesner, R. A.; Murphy, R. B.; Repasky, M. P.; Frye, L. L.; Greenwood, J. R.; Halgren, T. A.; Sanschagrin, P. C.; Mainz, D. T. Extra Precision Glide: Docking and Scoring Incorporating a Model of Hydrophobic Enclosure for Protein-Ligand Complexes. *J. Med. Chem.* **2006**, *49* (21), 6177−6196.
(50) Willoughby, P. H.; Jansma, M. J.; Hoye, T. R. A Guide to Small-Molecule Structure Assignment through Computation of (1H and 13C) NMR Chemical Shifts. *Nat. Protoc.* **2014**, *9* (3), 643−660.
(51) Mohamadi, F.; Richards, N. G. J.; Guida, W. C.; Liskamp, R.; Lipton, M.; Caufield, C.; Chang, G.; Hendrickson, T.; Still, W. C. Macromodel—an Integrated Software System for Modeling Organic and Bioorganic Molecules Using Molecular Mechanics. *J. Comput. Chem.* **1990**, *11* (4), 440−467.
(52) Banks, J. L.; Beard, H. S.; Cao, Y.; Cho, A. E.; Damm, W.; Farid, R.; Felts, A. K.; Halgren, T. A.; Mainz, D. T.; Maple, J. R.; Murphy, R.; Philipp, D. M.; Repasky, M. P.; Zhang, L. Y.; Berne, B. J.; Friesner, R. A.; Gallicchio, E.; Levy, R. M. Integrated Modeling Program, Applied Chemical Theory (IMPACT). *J. Comput. Chem.* **2005**, *26* (16), 1752−1780.
(53) Lu, C.; Wu, C.; Ghoreishi, D.; Chen, W.; Wang, L.; Damm, W.; Ross, G. A.; Dahlgren, M. K.; Russell, E.; Von Bargen, C. D.; Abel, R.; Friesner, R. A.; Harder, E. D. OPLS4: Improving Force Field Accuracy on Challenging Regimes of Chemical Space. *J. Chem. Theory Comput.* **2021**, *17* (7), 4291−4300.
(54) Allinger, N. L. Conformational Analysis. 130. MM2. A Hydrocarbon Force Field Utilizing V1and V2Torsional Terms. *J. Am. Chem. Soc.* **1977**, *99* (25), 8127−8134.
(55) Allinger, N. L.; Yuh, Y. H.; Lii, J. H. Molecular Mechanics. The MM3 Force Field for Hydrocarbons. 1. *J. Am. Chem. Soc.* **1989**, *111* (23), 8551−8566.
(56) Weiner, P. K.; Kollman, P. A. AMBER: Assisted Model Building with Energy Refinement. A General Program for Modeling Molecules and Their Interactions. *J. Comput. Chem.* **1981**, *2* (3), 287−303.
(57) Halgren, T. A. Merck Molecular Force Field. I. Basis, Form, Scope, Parameterization, and Performance of MMFF94. *J. Comput. Chem.* **1996**, *17* (5−6), 490−519.
(58) Sharapa, D. I.; Genaev, A.; Cavallo, L.; Minenkov, Y. A Robust and Cost-Efficient Scheme for Accurate Conformational Energies of Organic Molecules. *ChemPhyschem* **2019**, *20* (1), 92−102.
(59) Bochevarov, A. D.; Harder, E.; Hughes, T. F.; Greenwood, J. R.; Braden, D. A.; Philipp, D. M.; Rinaldo, D.; Halls, M. D.; Zhang, J.; Friesner, R. A. Jaguar: A High-Performance Quantum Chemistry Software Program with Strengths in Life and Materials Sciences. *Int. J. Quantum Chem.* **2013**, *113* (18), 2110−2142.
(60) Walker, M.; Harvey, A. J. A.; Sen, A.; Dessent, C. E. H. Performance of M06, M06-2X, and M06-HF Density Functionals for Conformationally Flexible Anionic Clusters: M06 Functionals Perform Better than B3LYP for a Model System with Dispersion and Ionic Hydrogen-Bonding Interactions. *J. Phys. Chem. A* **2013**, *117* (47), 12590−12600.
(61) Brameld, K. A.; Kuhn, B.; Reuter, D. C.; Stahl, M. Small Molecule Conformational Preferences Derived from Crystal Structure Data. A Medicinal Chemistry Focused Analysis. *J. Chem. Inf. Model* **2008**, *48* (1), 1−24.

https://doi.org/10.1021/acsomega.4c09421
ACS Omega 2025, 10, 5795−5808

(62) Hawkins, P. C. D. Conformation Generation: The State of the Art. *J. Chem. Inf. Model* **2017**, *57* (8), 1747−1756.
(63) Bursch, M.; Mewes, J.-M.; Hansen, A.; Grimme, S. Best-Practice DFT Protocols for Basic Molecular Computational Chemistry**. *Angew. Chem.* **2022**, *134* (42), No. e202205735.
(64) Wei, Y.; Debnath, S.; Weber, J. L.; Mahajan, A.; Reichman, D. R.; Friesner, R. A. Scalable Ab Initio Electronic Structure Methods with Near Chemical Accuracy for Main Group Chemistry. *J. Phys. Chem. A* **2024**, *128* (28), 5796−5807.
(65) Bogojeski, M.; Vogt-Maranto, L.; Tuckerman, M. E.; Müller, K. R.; Burke, K. Quantum Chemical Accuracy from Density Functional Approximations via Machine Learning. *Nat. Commun.* **2020**, *11* (1), 1−11.
(66) Lin, L.; Olson, M. E.; Sugane, T.; Turner, L. D.; Tararina, M. A.; Nielsen, A. L.; Kurbanov, E. K.; Pellett, S.; Johnson, E. A.; Cohen, S. M.; Allen, K. N.; Janda, K. D. Catch and Anchor Approach to Combat Both Toxicity and Longevity of Botulinum Toxin A. *J. Med. Chem.* **2020**, *63* (19), 11100−11120.
(67) Weeks, S. D.; Drinker, M.; Loll, P. J. Ligation Independent Cloning Vectors for Expression of SUMO Fusions. *Protein Expr. Purif.* **2007**, *53* (1), 40.
(68) Kabsch, W. Automatic Processing of Rotation Diffraction Data from Crystals of Initially Unknown Symmetry and Cell Constants. *J. Appl. Crystallogr.* **1993**, *26* (6), 795−800.
(69) McCoy, A. J.; Grosse-Kunstleve, R. W.; Adams, P. D.; Winn, M. D.; Storoni, L. C.; Read, R. J. Phaser Crystallographic Software. *J. Appl. Crystallogr.* **2007**, *40* (4), 658−674.
(70) Adams, P. D.; Grosse-Kunstleve, R. W.; Hung, L. W.; Ioerger, T. R.; McCoy, A. J.; Moriarty, N. W.; Read, R. J.; Sacchettini, J. C.; Sauter, N. K.; Terwilliger, T. C. P. Building New Software for Automated Crystallographic Structure Determination. *Acta Crystallogr. D Struct Biol.* **2002**, *58* (11), 1948−1954.
(71) Emsley, P.; Cowtan, K. Coot: Model-Building Tools for Molecular Graphics. *Acta Crystallogr. D Struct. Biol.* **2004**, *60* (12), 2126−2132.
(72) DeLano, W. *The PyMOL Molecular Graphics System*; Schrödinger, LLC

https://doi.org/10.1021/acsomega.4c09421
ACS Omega 2025, 10, 5795−5808